Direct numerical simulation of evaporating droplets

Jan Schlottke *, Bernhard Weigand

*Institut für Thermodynamik der Luft- und Raumfahrt (ITLR), Universität Stuttgart, Pfaffenwaldring 31,
70569 Stuttgart, Germany*

Abstract

A model for the three-dimensional direct numerical simulation of evaporating, deforming droplets in incompressible flow is presented. It is based on the volume-of-fluid method and is therefore capable of capturing very strong deformations. The evaporation rate is computed based on the vapour mass fraction and the PLIC reconstruction of the surface. Emphasis is put on the correct calculation of the velocities of the gaseous and liquid phase at the interface which is very important for cases with high mass transfer rates and thus high Stefan flow. It is accomplished by the use of an iterative algorithm that enforces a divergence constraint in cells containing the interface.

Validation comprises a 1D test case for interfacial mass transfer, droplet collisions and oscillations as well as calculation of Sherwood numbers for two different cases of evaporating droplets where low and high mass transfer rates occur. Comparison with data from the literature shows good agreement of the obtained results.

The simulation of a strongly deformed water droplet in a flow at a high Reynolds and Weber number is used to demonstrate the capabilities of the presented method. The emerging flow field in the wake of the droplet is very complex and three-dimensional.

© 2008 Elsevier Inc. All rights reserved.

Keywords: VOF; Evaporation; DNS; Stefan flow; Deformed droplets; Multiphase flow

1. Introduction

Heat and mass transfer across the liquid interface of multiphase flows is of extensive importance to many scientific and technical applications. The growth of raindrops due to condensation is a prominent example of these phenomena taking place in nature, whereas the evaporation of droplets during the combustion of fuel sprays in automotive engines or gas turbines has been subject to a large number of investigations in engineering. Another example is the process of droplets impinging on hot surfaces. It needs to be understood in order to assess the occurrence of thermal stresses in, for instance, lambda probes and serves as a good example of the complex interaction between the surrounding flow field, deformation of the free surface and heat/mass transfer across the liquid interface. In general, the small scales and high velocities hinder experimental access to

* Corresponding author. Tel.: +49 711 68562314; fax: +49 711 68562317.
  E-mail address: jan.schlottke@itlr.uni-stuttgart.de (J. Schlottke).

these topics, whereby numerical simulation of the mentioned phenomena has received considerable attention in the past.

Looking at the evaporation of sprays, the breakup-process can lead to strongly 3D deformed droplets with high velocities relative to the surrounding gas. The resulting high Reynolds numbers ($Re_D = D\rho u/\mu$) require a three-dimensional and transient numerical approach due to the complex flow field (the flow around droplets with a Reynolds number $Re_D > 270$ is fully 3D and unsteady) and lead to high computational costs.

The actual process of evaporation can be treated using the analogy of heat and mass transfer for low mass transfer rates only; it is therefore applicable to atmospheric phenomena, for example [16]. However, industrial processes (high-temperature environment) can lead to high mass transfer rates where the mass transfer needs to be considered separated from heat transfer, taking into account the Stefan flow.

The simulation of a multiphase flow with free interfaces still is one of the big challenges in CFD despite decades of work on that topic. Difficulties are, among others, the exact localization of the interface, calculation of surface tension and the high variation of fluid properties which can be three orders of magnitude (e.g. density ratio of water/air). The numerical method should be capable of maintaining a sharp interface without smearing it over a couple of cells due to numerical diffusion. Furthermore, the ability to cover strong topological changes including break-up and coalescence is desired, whereas the conservation of mass should still be guaranteed. Two different classes of methods have been developed in the past to deal with the mentioned tasks: *tracking* and *capturing methods*. *Tracking methods* are the moving mesh, front tracking, boundary integral and particle schemes. They are of Lagrangian type, the interface position is indicated by a Lagrangian marker which could be a particle or a polygon, etc. *Capturing methods* on the other hand are continuum advection, volume tracking, level set and phase field method schemes. Here the interface is captured from a function relating to the phases more than to the interface. A detailed overview of these schemes can be found in [17].

Renksizbulut and others [30,27] have used a *moving mesh method* for the computation of evaporation rates, focusing on droplets. The method is a *mixed method* with moving meshes only in the subset of the grid near the interface whereas the rest of the grid is a fixed Eulerian one. He used the method to determine the influence of variable properties on evaporation [28]. A disadvantage of the model is its limitation to 2D axisymmetric problems and small deformations. Haywood et al. used their model described in [11] to simulate the transient evaporation process of deformed droplets [12]. The model is similar to the one mentioned before and also limited to two-dimensional cases.

Juric and Tryggvason extended the *front tracking method* described in [45] for boiling flows [15].

Son and Dhir developed a model for boiling flow based on the *level set* approach [43,40]. *Level set methods* employ an additional transport variable representing the distance to the phase interface. They are capable of resolving arbitrary changes of the interfaces including break-up and coalescence. One big disadvantage of the original *level set* method is that conservation of liquid mass can not be guaranteed. This issue has been addressed by various authors, amongst others by Enright et al. [3] with their *particle level set* method or by Sussman et al. [42,41] with their coupled level set and volume of fluid method (CLSVOF), improving mass conservation significantly.

A method using the volume-of-fluid (VOF) approach for boiling flow was presented by Welch and Wilson [46]. VOF enables the scientist to detect any changes of topology and is in addition conservative due to its formulation. Welch and Wilson used the heat flux across the interface in order to calculate the mass of the phase changing liquid. They applied their method to a horizontal film-boiling problem in 2D.

Davidson and Rudman presented their VOF-based algorithm for the calculation of transport processes across deforming interfaces, using the analogy between heat and mass transfer [2]. The algorithm is limited to axisymmetric cases and does not consider volume changes due to phase change.

Jung and Sato conducted three-dimensional direct numerical simulations of a high Schmidt number flow over a droplet [14]. They employed a moving, unstructured mesh consisting of prisms at the interface to resolve the viscous boundary layer and tetrahedral cells in the remaining domain. Additional thin layer-cells inside the layer of prism-cells attached to the interface were used for calculation of mass transfer.

Another *level set* based approach to the topic of evaporation was shown by Tanguy et al. [44]. They utilized the Ghost Fluid Method [4] to enable the use of high order discretization schemes at the interface. By developing a model to calculate the interface velocities considering the volume change due to evaporation they were

able to cover the physical effects related to the Stefan flow. The calculations have been done in 2D and have not yet been validated against experimental data or correlations from the literature.

Gibou et al. [5] presented a similar method based on *level set* and Ghost Fluid, as well. They preserve the discontinuity of all variables but the viscosity which is smoothed across the interface. The method was applied to simulate film boiling in 2D.

Nikolopoulos et al. numerically investigated the behaviour of liquid droplets impinging onto a hot substrate using the VOF-method and adaptive mesh refinement [23]. They were able to predict the levitation of the drops above the Leidenfrost temperature and to calculate parameters of the splashing process below the Leidenfrost point.

Taking into account the requirements for the simulation of spray evaporation – namely strong deformations of the interface including break-up and coalescence and a complex, three-dimensional surrounding flow field –, the VOF-method seems to be a good choice to deal with those challenges. The work of the present paper is therefore based on the code FS3D (**F**ree **S**urface **3D**) [33] for isothermal, incompressible two-phase flows in 3D. Its efficiency and ability to simulate highly dynamic processes was proven in [35] for a splashing droplet and in [34] for droplet collisions. The code was extended by Hase to account for heat transfer [8]; the calculation of heat transfer of strongly deformed droplets was done in [9,10]. A simple evaporation model was implemented by Hase, having the disadvantage of being based on empirical parameters [7]. In the recent past FS3D was employed to simulate the primary breakup of turbulent jets [38]. Special features of FS3D are its efficient multigrid solver, its complete parallelization via OpenMP and MPI with domain decomposition and vectorization, thus facilitating the computation of large problems.

The present paper will focus on the direct numerical simulation of 3D deformed droplets in a flow. To the best knowledge of the author such calculations have not been reported before in the literature.

2. Mathematical formulation

2.1. Phase representation by the VOF method

We describe below our method for handling surface deformation in the presence of three phases. The method is broadly based on the volume-of-fluid method [13] but there are some important enhancements with regard to volume conservation and interface velocity. First, the formulation for two phase flows without phase change is presented; it will be expanded to a third phase including phase change subsequently.

In order to distinguish between two phases, the additional field variable f_1, which shall be

$$f_1(\mathbf{x}, t) = \begin{cases} 0 & \text{in the gaseous phase} \\ 0 < f_1 < 1 & \text{in cells containing a part of the interface} \\ 1 & \text{in the liquid phase} \end{cases} \tag{1}$$

and represents the volume fraction of the liquid phase, is utilized. An explaining illustration is given in Fig. 1.

The function f_1 is transported across the computed domain by [33]

$$\frac{\partial f_1}{\partial t} + \nabla \cdot (f_1 \mathbf{u}) = 0. \tag{2}$$
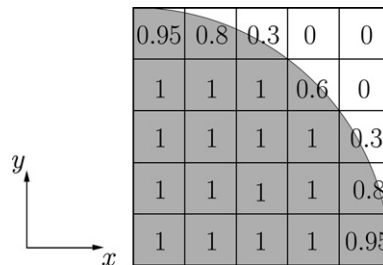

Fig. 1. Fluid representation by the f_1 variable.

A crucial requirement to the successful advection of f_1 is a sharp interface and the exact knowledge of its position, otherwise f_1 gets smudged across several cell layers due to numerical diffusion. This task is met by reconstructing the interface using the PLIC (Piecewise Linear Interface Calculation) algorithm [32]. The reconstruction is done on a geometrical basis and serves for the determination of the liquid and gaseous fluxes across the cell faces.

In order to account for a third phase a second VOF-variable is introduced: f_2 is the volume fraction of vapour. It is assumed to be insoluble inside the liquid phase but there is diffusion in the gaseous phase.

We start with the transport equation of one component i in a multicomponent gas mixture as given by [22]:

$$\frac{\partial \rho_{p,i}}{\partial t} + \nabla \cdot (\rho_{p,i}\mathbf{u}) = \nabla \cdot (\rho \mathcal{D}_{12}\nabla X_i) + \dot{m}_i''', \tag{3}$$

where $\rho_{p,i}$ is the partial density, $X_i = \rho_{p,i}/\rho$ is the mass fraction of component i, $\mathcal{D}_{12}$ is the binary diffusion coefficient and $\dot{m}_i'''$ is the volumetric source. $\rho_{p,i}$ can be expressed by the VOF-variable f_i

$$\rho_{p,i} = \frac{m_i}{V} = \frac{\rho_i V_i}{V} = \frac{\rho_i f_i V}{V} = \rho_i f_i, \tag{4}$$

leading to

$$\frac{\partial \rho_i f_i}{\partial t} + \nabla \cdot (\rho_i f_i \mathbf{u}) = \nabla \cdot \left(\rho \mathcal{D}_{12}\nabla\left(\frac{\rho_i f_i}{\rho}\right)\right) + \dot{m}_i'''. \tag{5}$$

Assuming that $\rho_i = $ const., it can be simplified to

$$\frac{\partial f_i}{\partial t} + \nabla \cdot (f_i \mathbf{u}) = \nabla \cdot \left(\rho \mathcal{D}_{12}\nabla\left(\frac{f_i}{\rho}\right)\right) + \frac{\dot{m}_i'''}{\rho_i} \tag{6}$$

and the transport equation of the vapour phase can be stated as

$$\frac{\partial f_2}{\partial t} + \nabla \cdot (f_2 \mathbf{u}_{gp}) = \nabla \cdot \left(\rho_{gp} \mathcal{D}_{vg}\nabla\left(\frac{f_2}{\rho_{gp}}\right)\right) + \frac{\dot{m}'''}{\rho_v}. \tag{7}$$

Here, $\mathcal{D}_{vg}$ is the binary diffusion coefficient of the vapour inside the gas, ρ_{gp} is the density of the gaseous phase and the last term reflects the production of vapour due to evaporation with $\dot{m}'''$ being the volumetric mass source of vapour and ρ_v the vapour density. The generation of volume as a result of the evaporation process requires the use of different transport velocities; the gaseous phase gets advected by $\mathbf{u}_{gp}$, the liquid phase by $\mathbf{u}_\Gamma$ (because of the high density ratios considered, the velocities of the interface and of the liquid phase are assumed to be equal). $\mathbf{u}_{gp}$ and $\mathbf{u}_\Gamma$ differ from each other only in cells containing a part of the interface, there is no need to discriminate in the residual domain. The calculation of these velocities and the volumetric vapour source will be described in detail in Section 3.

Neglecting the change of density inside the gaseous phase due to $\rho_v \approx \rho_g$, Eq. (7) can further be simplified to (see [7] for a detailed derivation):

$$\frac{\partial f_2}{\partial t} + \nabla \cdot (f_2 \mathbf{u}_{gp}) = \nabla \cdot (\mathcal{D}_{vg}\nabla f_2) + \frac{\dot{m}'''}{\rho_v}. \tag{8}$$

The transport equation of the liquid phase finally reads

$$\frac{\partial f_1}{\partial t} + \nabla \cdot (f_1 \mathbf{u}_\Gamma) = \frac{-\dot{m}'''}{\rho_l}, \tag{9}$$

where ρ_l is the liquid density.

The VOF-variables are used to compute local fluid properties by applying the *one-field* formulation, resulting in

$$\rho(\mathbf{x},t) = \rho_l f_1(\mathbf{x},t) + \rho_v f_2(\mathbf{x},t) + (1 - f_1(\mathbf{x},t) - f_2(\mathbf{x},t))\rho_g \tag{10}$$

for the local density, for example. Other properties like the dynamic viscosity μ or the heat conductivity λ are calculated analogously; however, the specific heat capacity c_p is mass averaged instead of volume averaged. In

the present paper, the fluid properties are assumed to be constant for a given case. This limitation will be overcome in the future by using temperature dependent properties.

2.2. Momentum equations

In the momentum equations

$$\frac{\partial(\rho\mathbf{u})}{\partial t} + \nabla \cdot (\rho\mathbf{u}) \otimes \mathbf{u} = -\nabla p + \rho\mathbf{k} + \nabla \cdot \mu[(\nabla\mathbf{u} + (\nabla\mathbf{u})^{\mathrm{T}})] + \mathbf{f}_\gamma \qquad (11)$$

$\mathbf{u}$ is the velocity of the one-field formulation ($\mathbf{u}_{\mathrm{gp}}$ and $\mathbf{u}_\Gamma$ are the transport velocities of the VOF-variables and only differ from $\mathbf{u}$ in cells containing the interface), p is the pressure and the term $\rho\mathbf{k}$ accounts for body forces, e.g. gravity. Surface tension, which is of major importance to the treatment of multiphase flows, is included as the volume force $\mathbf{f}_\gamma$. Following the conservative model presented by Lafaurie et al. [19] this force is computed using the smoothed VOF variable $\tilde{f}_1$ by

$$\mathbf{f}_\gamma = \nabla \cdot (\sigma a_\Gamma[\mathbf{I} - \hat{\mathbf{n}}_\Gamma\hat{\mathbf{n}}_\Gamma]) \qquad (12)$$

with σ being the surface tension, $a_\Gamma = |\nabla\tilde{f}_1|$ the surface density and $\hat{\mathbf{n}}_\Gamma = \nabla\tilde{f}_1/|\nabla\tilde{f}_1|$ the unit normal vector on the surface. Smoothing of the VOF variable is necessary in order to minimize the occurrence of parasitic currents due to discretization errors. It is only performed for the calculation of $\mathbf{f}_\gamma$ and has no influence on the actual f_1-distribution. As proposed by [1], $\tilde{f}_1$ is computed using the tensor product of a quadratic B-spline. The coefficients of the smoothing operator **B2** only differ from zero in the 26 surrounding cells and the considered cell itself. By defining $\mathbf{i} = (i, j, k)$ and $\mathbf{j} = (r, s, t)$, the smoothing operation can be expressed as

$$\tilde{f}_{1,\mathbf{i}} = \sum_{\mathbf{j} \in S_{B2}} \mathbf{B2}(\mathbf{i}, \mathbf{j}) f_{1,\mathbf{i}+\mathbf{j}} \qquad (13)$$

with

$$S_{B2} = \{[-1, 0, 1] \times [-1, 0, 1] \times [-1, 0, 1]\}. \qquad (14)$$

The smoothing operator is given by

$$\mathbf{B2} = \frac{1}{512}\begin{bmatrix} 1 & 6 & 1 \\ 6 & 36 & 6 \\ 1 & 6 & 1 \end{bmatrix}_{t=-1}, \quad \frac{1}{512}\begin{bmatrix} 6 & 36 & 6 \\ 36 & 216 & 36 \\ 6 & 36 & 6 \end{bmatrix}_{t=0}, \quad \frac{1}{512}\begin{bmatrix} 1 & 6 & 1 \\ 6 & 36 & 6 \\ 1 & 6 & 1 \end{bmatrix}_{t=1}. \qquad (15)$$

The pressure p in Eq. (11) is computed by projecting the emerging velocity field onto one fulfilling the continuity equation (see below) and solving the resulting Poisson equation.

2.3. Continuity equation

In contrast to two phase flows without phase change (and no solubility of one phase inside the other) where the divergence-free condition of the velocity field has to be satisfied for incompressible flows, new volume is generated by evaporation or volume vanishes due to condensation, therefore volume sources or sinks are found at the interface. An obvious approach is

$$\nabla \cdot \mathbf{u} = -\dot{m}'''\left(\frac{1}{\rho_{\mathrm{v}}} - \frac{1}{\rho_{\mathrm{l}}}\right), \qquad (16)$$

where a volume balance is given on the right hand side. This expression has been used by various authors, e.g. by Son and Dhir [40] in the level-set framework. Gibou et al. [5] and Tanguy et al. [44], both using a combination of the level-set method and Ghost Fluid method, defined their velocity jump conditions in a similar war. For the VOF-method however, $\mathbf{u}$, reflecting the velocity field of the one-field formulation, is mass averaged and therefore generally not volume conservative. Hence Eq. (16) is valid only for few cases which will be pointed out in the following.

In order to get a better understanding of this fact, first the definitions of the volume weighted and the mass weighted velocity are presented. Fig. 2 shows the general case of a partly filled cell. $f_{y,j-1/2}$ reflects the wetted portion of face $j-1/2$, the non-wetted portion is therefore $1 - f_{y,j-1/2}$. The volume weighted velocity in the direction of y is given by

$$v_{\text{vol},j-1/2} = v_{\Gamma,j-1/2}f_{y,j-1/2} + v_{\text{gp},j-1/2}(1 - f_{y,j-1/2}), \tag{17}$$

whereas the mass weighted velocity also contains the densities of the phases (the subscript gp denotes the gaseous phase, that is vapour and inert gas):

$$v_{\rho,j-1/2} = \frac{v_{\Gamma,j-1/2}f_{y,j-1/2}\rho_{\text{f}} + v_{\text{gp},j-1/2}(1 - f_{y,j-1/2})\rho_{\text{gp}}}{f_{y,j-1/2}\rho_{\text{f}} + (1 - f_{y,j-1/2})\rho_{\text{gp}}}. \tag{18}$$

In case of fully wetted or completely empty cell faces, there is only one important transport velocity – either the velocity of the liquid phase (in case $f_y = 1$) or the velocity of the gaseous phase ($f_y = 0$). Then both definitions for v_ρ and v_{vol} lead to the same velocity and Eq. (16) is valid.

For the more common case of partly wetted cell faces, v_ρ and v_{vol} differ due to the large density ratio encountered in most observed flows (e.g. water–air: $\rho_{\text{f}}/\rho_{\text{gp}} \approx 1000$). Here, Eq. (16) is not valid anymore because the divergence of **u** does not reflect the balance of volume fluxes across the cell faces.

The problem is handled by computing a virtual velocity field **u**∗ based on the velocities of the interface and the gaseous phase, **u**$_\Gamma$ and **u**$_{\text{gp}}$, and employing its divergence to the actual continuity equation

$$\nabla \cdot \mathbf{u} = \nabla \cdot \mathbf{u}^*. \tag{19}$$

The calculation of **u**$_\Gamma$, **u**$_{\text{gp}}$ and **u**∗ will be described in detail in the following section. Note that volume changes due to diffusion are not taken into account.

2.4. Energy equation

Neglecting the production of thermal energy by viscous dissipation, the energy equation in temperature formulation is given by [7]

$$\frac{\partial}{\partial t}(\rho c_{\text{p}}T) + \nabla \cdot (\rho c_{\text{p}}\mathbf{u}T) = \nabla \cdot (\lambda \nabla T) + T_0 \left[\frac{\partial}{\partial t}(\rho c_{\text{p}}) + \nabla \cdot (\rho c_{\text{p}}\mathbf{u}) \right] + \rho_{\text{v}}\Delta h_{\text{v}} \frac{\dot{m}'''}{\rho_{\text{v}}}, \tag{20}$$

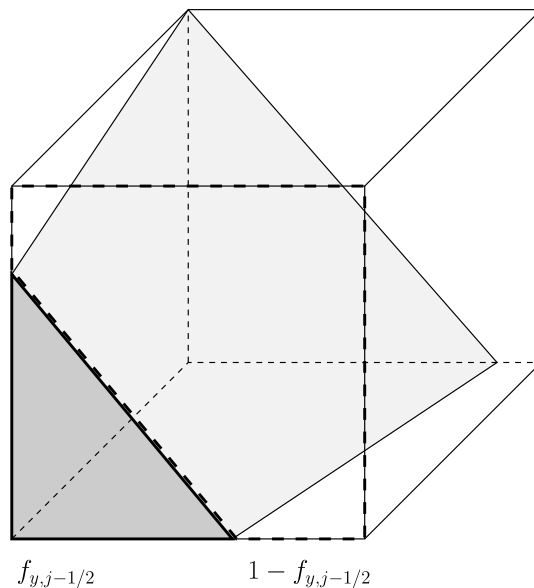$$f_{y,j-1/2} \qquad\qquad 1 - f_{y,j-1/2}$$

Fig. 2. Definition of mass averaged and volume averaged velocities.

where T denotes the temperature, T_0 is the reference temperature for zero enthalpy and Δh_v the latent heat of the evaporating fluid. For further details concerning the implementation and validation see [8].

3. Numerical details

3.1. Computational grid

The spatial discretization is based on a cartesian grid using a staggered arrangement of the variables (MAC-grid [6]). All scalar variables (f_1, f_2, p, T) are stored at the cell centre whereas the velocities are stored at the centre of the cell faces. Discrete values are assigned with the subscripts i, j, k in order to express the position of the considered cell in the x-, y- and z-direction, respectively.

3.2. Calculation of $\dot{m}'''$

The volumetric mass source of vapour $\dot{m}'''$ is calculated in cells containing the interface only. The criterion for a cell to contain the interface is that f_1 has to satisfy the condition

$$0.0 + \varepsilon < f_1 < 1.0 - \varepsilon \tag{21}$$

with ε being a small number ($\varepsilon = 10^{-6}$), hence avoiding the evaporation either in cells containing only very small amounts of f_1 or in cells that are almost completely filled with liquid.

The local area specific mass source of vapour is calculated based on the gradient of vapour mass fraction X_v normal to the surface. Following the derivation in [16] it can be stated as

$$\dot{m}'' = \frac{\mathcal{D}_{vg}\rho_{gp}}{1 - X_v} \nabla X_v \hat{\mathbf{n}}_\Gamma, \tag{22}$$

where ρ_{gp} is the local density of the gaseous phase which is computed by the density of gas and vapour contained inside the cell:

$$\rho_{gp} = \frac{\rho_g(1 - f_1 - f_2) + \rho_v f_2}{1 - f_1}. \tag{23}$$

Now the vapour mass fraction can be determined by

$$X_v = \frac{f_2}{1 - f_1} \frac{\rho_v}{\rho_{gp}} \tag{24}$$

in each cell containing the gaseous phase.

The vapour pressure at the surface is assumed to be the saturation pressure. It depends primarily on the surface temperature (the temperature of the cell containing the interface) and is estimated by the Wagner equation which is given in Appendix A. This pressure is subsequently used to calculate the vapour mass fraction at the surface, assuming the whole cell containing the interface to be at saturation condition. As derived by Mills [22], the mole fraction of saturated vapour can be stated as

$$x_{v,sat} = \frac{p_{v,sat}}{p_{stat}} \tag{25}$$

with $p_{v,sat}$ and p_{stat} being the saturation and static pressure, respectively. The mass fraction of saturated vapour at the interface is finally calculated by applying the following relation, containing the molecular weights of the vapour M_v and the inert gas M_g:

$$X_{v,sat} = x_{v,sat} \frac{M_v}{M_{gp,sat}} = x_{v,sat} \frac{M_v}{x_{v,sat}M_v + (1 - x_{v,sat})M_g}. \tag{26}$$

Knowing the mass fraction of vapour at the surface as well as in the residual domain containing the gaseous phase, one can now calculate its gradient. The procedure will be illustrated on basis of the x-component exemplarily. In order to account for the fact that the saturation condition is actually encountered at the
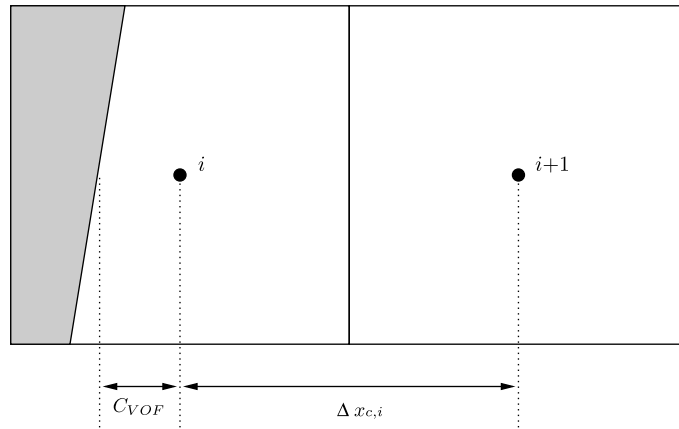
Fig. 3. The corrective offset C_{VOF}.

surface only, the discretization of the gradient is extended by a corrective offset C_{VOF}. A sketch explaining this offset is shown in Fig. 3. C_{VOF} is obtained on basis of the PLIC reconstruction and thus reflects the geometry of the surface. Considering

$$\left(\frac{\partial X_{\mathrm{v}}}{\partial x}\right)_i = \frac{X_{\mathrm{v},i+1} - X_{\mathrm{v,sat},i}}{\Delta x_{\mathrm{c},i} + C_{\mathrm{VOF}}}, \tag{27}$$

where $\Delta x_{\mathrm{c},i}$ denotes the distance between the two centres of the neighbouring cells i and $i+1$, it becomes apparent that this offset augments the denominator in case of a rather empty cell where the distance between the cell $i+1$ and the surface is bigger whereas it reduces the denominator in case of a rather full cell.

Now all requirements are met to calculate Eq. (22). The volumetric mass source of vapour is obtained by multiplying $\dot{m}''$ with the local interface density a_Γ:

$$\dot{m}''' = a_\Gamma \dot{m}''. \tag{28}$$

It is important to point out the necessity to calculate the local interface density based on the PLIC reconstruction instead of employing the relationship $a_\Gamma = |\nabla f_1|$ which represents the complete interfacial area only globally.

In the case of cells containing almost no liquid ($f_1 \approx 0$), the mass source is limited to

$$\dot{m}''' = \frac{f_1 \rho_1}{\Delta t} \tag{29}$$

in order to avoid undershoots of the f_1-variable.

3.3. Velocities of the liquid and the gaseous phase

The correct computation of the velocities found at the interface is essential to an exact and stable treatment of the emerging flow field. The occurence of different velocities of the gaseous and the liquid phase due to the volume change inherent to evaporation is depicted in Fig. 4. It shows the simple case of the surface normal being parallel to the x-axis with one fully wetted cell face ($i-1/2$) and one cell face with only the gaseous phase flow ($i+1/2$). Here, the fluid is advected across the left cell face by the surface velocity $u_{\Gamma,i-1/2}$ which is simultaneously the mass averaged velocity $u_{\rho,i-1/2}$ and the volume averaged velocity $u_{\mathrm{vol},i-1/2}$. On the right face, the velocity of the gaseous phase $u_{\mathrm{gp},i+1/2}$ as well as $u_{\rho,i+1/2}$ and $u_{\mathrm{vol},i+1/2}$ coincide. The relationship between those velocities results from balancing the fluxes and the production of volume at the surface in

$$u_{\mathrm{gp},i+1/2} - u_{\Gamma,i-1/2} = \dot{m}''' \left(\frac{1}{\rho_{\mathrm{v}}} - \frac{1}{\rho_1}\right) \Delta x_i, \tag{30}$$
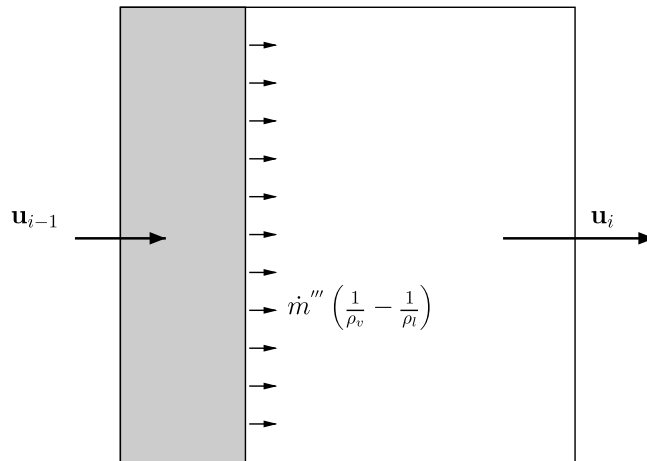
Fig. 4. Velocities of the gaseous and liquid phase, part 1.

where Δx_i indicates the edge length of cell i. Here the volume source is assumed to affect the velocity component perpendicular to the surface only.

In Fig. 5 a more general but also more complicated case with an arbitrarily oriented surface and partially wetted cell faces is illustrated. The determination of the velocities is now much more complicated. On the one hand a combination of the velocities has to be found that satisfies the volume balance inside the cell, on the other hand the influence of the volume sources inside the neighbouring cells has to be considered as well.

These difficulties are handled by the use of an iterative algorithm which is presented below. It calculates preliminary velocities of the liquid and the gaseous phase at the interface and detects the error relating to the divergence constraint. This error is distributed subsequently in order to obtain the desired velocity field. The algorithm consists of the following steps:

(1) *Calculation of preliminary velocities* $\mathbf{u}'_\Gamma$ *and* $\mathbf{u}'_{\mathrm{gp}}$. As already stated above, the volume source $\dot{m}''' \left(\frac{1}{\rho_v} - \frac{1}{\rho_l} \right)$ is assumed to affect the different velocities according to the components of the unit normal vector inside the cell. This means, for example, that the v- and w-velocities are not changed if the surface normal vector points in the direction of u. Furthermore, in case that two neighbouring cells contain the interface (and thus evaporation occurs), the volume sources and normal vectors which are defined at the cell centres are
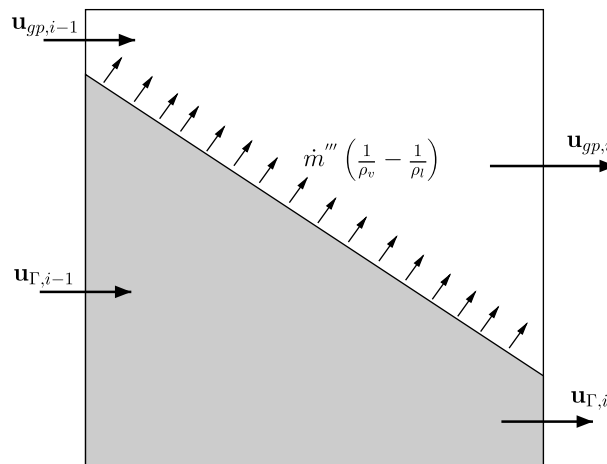

Fig. 5. Velocities of the gaseous and liquid phase, part 2.

interpolated to the cell faces. Velocities on cell faces that are completely wetted (mainly adjacent to cells filled by liquid with $f_1 = 1$) are not changed. Starting with a volume flux balance across the non-wetted portion of face $(i + 1/2)$ (see Fig. 5), one obtains

$$A(1 - f_x)u_\Gamma + V\overline{\dot{m}'''}\left(\frac{1}{\rho_v} - \frac{1}{\rho_l}\right)\overline{\left(\frac{n_x}{|\mathbf{n}|}\right)} = A(1 - f_x)u_{gp}, \tag{31}$$

where A denotes the area of face $(i + 1/2)$ and V the volume of cell i. After combination with Eq. (18) and simplification, the equations for $\mathbf{u}'_\Gamma$ and $\mathbf{u}'_{gp}$ read

$$\mathbf{u}'_\Gamma = \mathbf{u}_\rho - \overline{\dot{m}'''}\Delta\mathbf{x}_c\left(\frac{n_x}{|\mathbf{n}|}\right)\left(\frac{1}{\rho_v} - \frac{1}{\rho_l}\right)\left(\frac{\rho_{gp}}{\rho}\right), \tag{32}$$

$$\mathbf{u}'_{gp} = \mathbf{u}_\rho + \overline{\dot{m}'''}\Delta\mathbf{x}_c\left(\frac{n_x}{|\mathbf{n}|}\right)\left(\frac{1}{\rho_v} - \frac{1}{\rho_l}\right)\left(\frac{\rho_l}{\rho}\right)\left(\frac{\mathbf{f}_A}{1 - \mathbf{f}_A}\right), \tag{33}$$

where $\mathbf{f}_A$ is the wetted portion of the cell faces and $\mathbf{u}_\rho$ is the mass weighted velocity obtained by the pressure correction of the last time step. They describe the dependency on the mass weighted velocity and the volume source.

(2) *Calculation of a preliminary volume weighted velocity* $\mathbf{u}'_{vol}$ *and its divergence error.* $\mathbf{u}'_\Gamma$ and $\mathbf{u}'_{gp}$ are now used to compute the preliminary volume weighted velocity:

$$\mathbf{u}'_{vol} = \mathbf{u}'_\Gamma\mathbf{f}_A + \mathbf{u}'_{gp}(1 - \mathbf{f}_A). \tag{34}$$

Its divergence $\nabla \cdot \mathbf{u}'_{vol}$ is compared to the desired divergence produced by evaporation and an error is computed for each cell containing the interface:

$$E_{(\nabla \cdot \mathbf{u}_{vol})} = \dot{m}'''\left(\frac{1}{\rho_v} - \frac{1}{\rho_l}\right) - \nabla \cdot \mathbf{u}'_{vol}. \tag{35}$$

(3) *Distribution of* $E_{(\nabla \cdot \mathbf{u}_{vol})}$ *and calculation of final values for* $\mathbf{u}_\Gamma$ *and* $\mathbf{u}_{gp}$. This error is distributed to the spatial directions according to the local unit normal vector of the surface. This is beneficial to the computational performance because each velocity component can now be treated independently, thus facilitating vectorization. One problem is that once the velocities at the faces of one cell (e.g. $u_{i-1/2}$ and $u_{i+1/2}$ for cell i) are adjusted to account for $E_{(\nabla \cdot \mathbf{u}_{vol})}$, these velocities are fixed and must not be changed by the neighbouring cells. It is overcome by the use of a "credit point"-system which rates all cells containing the interface by figuring out if there are unchangeable neighbours (fully wetted faces, see above) and on basis of the f_1-variable (the fuller, the higher the priority of the considered cell) and identifies the best sequence in which the velocities are computed. Looking at the examples given in Fig. 6, the algorithm starts calculating the velocities on the faces of cell i in both cases and then moves to the adjacent cells. The final volume weighted velocities u_{vol} for cell i are obtained by

$$u_{vol,i-1/2} = u'_{vol,i-1/2} + E_{(\nabla \cdot \mathbf{u}_{vol}),i}\left(\frac{n_x}{|\mathbf{n}|}\right)_i\Delta x_i\left(\frac{\frac{1}{\rho_{i-1/2}}}{\frac{1}{\rho_{i+1/2}} + \frac{1}{\rho_{i-1/2}}}\right), \tag{36}$$

$$u_{vol,i+1/2} = u'_{vol,i+1/2} + E_{(\nabla \cdot \mathbf{u}_{vol}),i}\left(\frac{n_x}{|\mathbf{n}|}\right)_i\Delta x_i\left(\frac{\frac{1}{\rho_{i+1/2}}}{\frac{1}{\rho_{i+1/2}} + \frac{1}{\rho_{i-1/2}}}\right) \tag{37}$$

if the velocities on both faces are changed. The last term provides a reasonable spreading of $E_{(\nabla \cdot \mathbf{u}_{vol})}$ so that velocities on barely wetted cell faces contribute more to the divergence of $\mathbf{u}_{vol}$ and vanishes if $\mathbf{u}_{vol}$ has to be changed on one face only. Now $\mathbf{u}_\Gamma$ and $\mathbf{u}_{gp}$ are computed by

$$\mathbf{u}_\Gamma = \mathbf{u}_{vol} + \overline{\dot{m}'''}\left(\frac{1}{\rho_v} - \frac{1}{\rho_l}\right)\Delta\mathbf{x}_c\left(\frac{n_x}{|\mathbf{n}|}\right)\left(\frac{\mathbf{f}_A}{1 - \mathbf{f}_A}\right), \tag{38}$$

$$\mathbf{u}_{gp} = \mathbf{u}_{vol} - \overline{\dot{m}'''}\left(\frac{1}{\rho_v} - \frac{1}{\rho_l}\right)\Delta\mathbf{x}_c\left(\frac{n_x}{|\mathbf{n}|}\right), \tag{39}$$
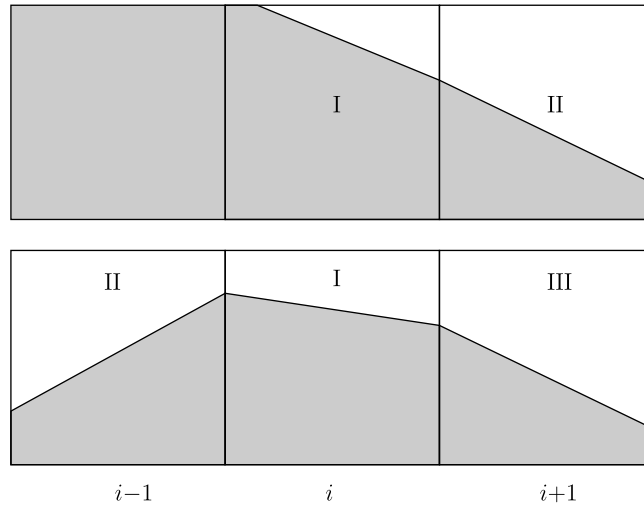
which results from combining Eq. (31) and (17).

Fig. 6. Sequence of calculating the velocities.

(4) *Calculation of $\mathbf{u}_\rho^*$ and the source of the continuity equation.* Finally, a mass weighted velocity field $\mathbf{u}_\rho^*$ is calculated with its definition given in Eq. (18)

$$\mathbf{u}_\rho^* = \mathbf{u}_\Gamma \mathbf{f}_A \rho_1 + \mathbf{u}_{gp}(1 - \mathbf{f}_A)\rho_{gp}. \tag{40}$$

Its divergence is employed as the source term for the continuity equation as given in Eq. (19).

3.4. Time integration

The accuracy of the time integration is of first order. The convective and diffusive transport terms are performed explicitly and the particular stability constraints are obeyed. For the advective transport, $\mathbf{u}$, $\mathbf{u}_\Gamma$ and $\mathbf{u}_{gp}$ are employed and the *Courant–Friedrichs–Levy* (CFL) stability condition is followed. When calculating the CFL number in cells containing the interface, one has to bear in mind that $\mathbf{u}_\Gamma$ and $\mathbf{u}_{gp}$ are only model velocities and not actual transport velocities. The transport velocities used for calculating the CFL number can be derived from the fluxes of the liquid and gaseous phase.

For the diffusive transport, stability constraints are

$$\frac{2\mu\Delta t}{\rho\Delta x^2} \leqslant 1, \quad \frac{2\lambda\Delta t}{\rho c_p\Delta x^2} \leqslant 1 \quad \text{and} \quad \frac{2\mathcal{D}_{vg}\Delta t}{\Delta x^2} \leqslant 1 \tag{41}$$

for the viscous transport, heat conduction and vapour diffusion, respectively. The explicit treatment of the diffusive terms limits the presented method to convective dominated problems. In the case of diffusive dominated problems (e.g. high-viscosity fluids), an implicit treatment of these terms would avoid stability problems but also implicate a higher computational effort.

The capillary time step constraint is

$$\frac{2\sqrt{\frac{\sigma\pi}{\rho_1+\rho_g}}\Delta t}{\Delta x^{3/2}} \leqslant 1. \tag{42}$$

The Poisson equation that arises from projecting the preliminary velocity field onto one fulfilling the divergence condition given in Eq. (19) is solved implicitly by a fast multigrid algorithm. The emerging velocity field at the next time level $\mathbf{u}^{n+1}$ serves for the calculation of $\mathbf{u}_\Gamma^{n+1}$ and $\mathbf{u}_{gp}^{n+1}$ as described in Section 3.3.

4. Results

A large number of very detailed validation cases have been run over the past decade for the in house code FS3D, ranging from colliding droplets over droplet wall interactions, splashing droplets, transient heat transfer in droplets and evaporation. The reader is referred to [34,21,35,10,7] for more details on this work.

For the present study, the capability of the presented method to properly account for the interfacial jump conditions and mass transfer was proven for a 1D test case where an analytical solution is available.

Further more, the correct implementation of surface tension and the ability to compute large deformations is shown by a brief comparison with the results of Pan and Suga [24] for colliding droplets with and without evaporation. In addition, the frequency of surface tension driven droplet oscillations is compared to an analytical solution.

Validation is then performed for evaporating droplets because of the relevance to spray modelling and the extensive investigations that have been done in the past in this field of work. Here, some qualitative results are shown which demonstrate the ability of the presented method to simulate the considered problems. Subsequent to this a quantitative comparison between numerical results and correlations from literature for both low and high mass transfer conditions is presented.

In order to demonstrate the power of the present code FS3D, the behaviour of a deformed droplet in an air stream at high Reynolds and Weber number is investigated.

4.1. Numerical setup

All calculations have been done on a three-dimensional cartesian grid.

The setup used for the 1D test case is described in the following section. The simulation of droplet collisions for comparison with Pan and Suga and the investigations on oscillation frequencies have been performed inside a rectangular domain with continuous boundary conditions.

The computational domain for evaporating droplets is shown schematically in Fig. 7 with a 2D cut through the centre of the droplet. In order to minimize the numerical effort a coordinate system moving at droplet speed with a damping zone at the outlet is used. This makes it possible to keep the droplet in the centre of the domain. The damping zone avoids back-flow into the computational domain at the outflow and was described in detail in [36]. On the left boundary an inflow condition with a uniform velocity distribution is used, the lateral boundary conditions are free slip conditions. The vapour variable f_2 was set to zero in the whole domain (dry air) at the beginning of the simulations.

The cell size of the employed grids has been selected in a way to capture the small scale features in the flow. For evaporation this means that the thermal and concentration boundary layer around the droplet had to be resolved.

4.2. Validation

4.2.1. 1D test case for interfacial mass transfer

The correct treatment of the jump conditions at the interface was judged considering the case of a laminar Couette flow with high mass transfer. The numerical setup, consisting of a non-moving liquid film at the bottom and the prescribed velocity u_∞ at the top with a distance of δ between interface and top boundary is depicted in Fig. 8. The liquid temperature T_s is kept constant during the simulation and determines the resulting mass transfer number $B_M = (X_{v,s} - X_{v,\infty})/(1 - X_{v,s})$. The vapour mass fraction $X_{v,\infty}$ is kept constant, too.
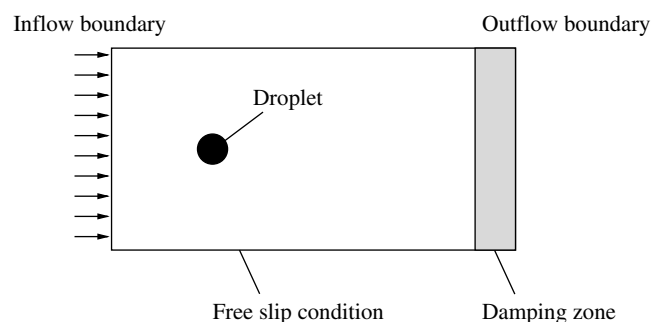

Fig. 7. Numerical setup.
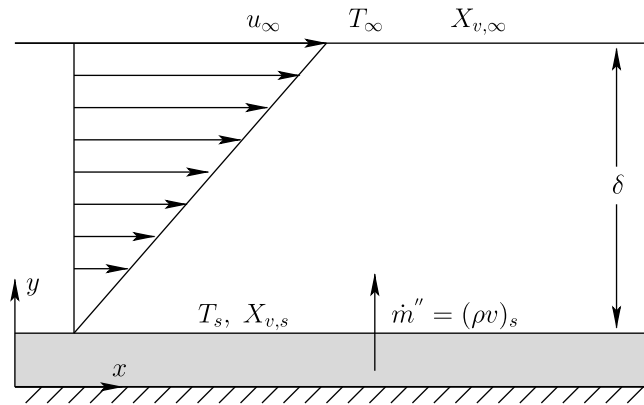
Fig. 8. Numerical setup of the 1D test case (couette flow).

The mass transfer conductance g is introduced according to [16] as

$$\dot{m}'' = g\frac{X_{v,s} - X_{v,\infty}}{1 - X_{v,s}} = gB_M. \tag{43}$$

Decreasing B_M results in vanishing mass transfer $\dot{m}'' \to 0$ and the parameter g^* is defined for this limiting case:

$$g^* = \lim_{B_M \to 0} \frac{\dot{m}''}{B_M}. \tag{44}$$

For the considered laminar Couette flow, the ratio g/g^* can be analytically proven to be only dependent on the mass transfer driving force B_M (see e.g. [16,22]), leading to

$$\frac{g}{g^*} = \frac{\ln(1 + B_M)}{B_M}. \tag{45}$$

Simulation results for water at different mass transfer numbers B_M (T_s ranging from 273 K to 362 K) are shown in Fig. 9, matching the analytical solution perfectly. This match demonstrates the ability of the presented method to calculate the interfacial mass transfer in terms of mass diffusion and the velocity v_s normal to the surface caused by the Stefan flow in a correct way.
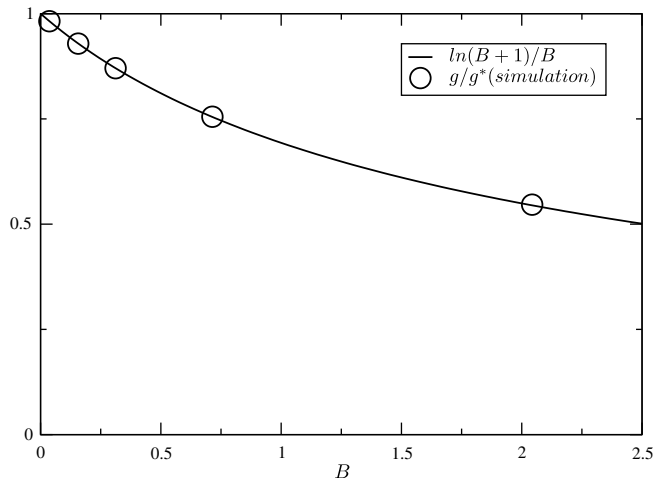

Fig. 9. Numerical results and analytical solution for the 1D test case.

4.2.2. Surface tension

Investigations on colliding water droplets have been conducted. The collision Weber number was $We_{collision} = (\rho_1 D_0 (2U_0)^2)/\sigma = 20$ and the impact parameter $\chi = b/D_0 = 0.05$. $2U_0$ is the relative velocity of the droplets, D_0 their initial diameter and b is the distance between the centres of the droplets projected onto the direction perpendicular to the relative velocity at the moment of impact. All material properties used are the ones given in [24]. In case of additional evaporation of the colliding droplets, the water temperature was chosen to be $T_1 = 293$ K. The outcome of the simulations with and without evaporation is presented in Fig. 10 together with the results of Pan and Suga. One can observe a good agreement of the results. Looking at the conducted calculations with and without evaporation, it can be noticed that the shape of the droplets is not substantially different for both cases.

For additional validation surface tension driven droplet oscillations were simulated. The simulations were performed starting with a non-moving ellipsoidal droplet with the polar radius being 50% bigger than the equatorial radii. The resulting periodic times were compared to those obtained by an analytical approach of Lamb [20] that is valid for small deformations and neglects the density of the surrounding gas. His formula for the angular frequency reads

$$\omega^2 = l(l-1)(l+2)\frac{\sigma}{\rho_1 R^3}. \tag{46}$$

The parameter l defines the mode of the oscillation and was selected $l = 2$ for ellipsoidal deformations. The periodic times T resulting from both simulations and Eq. (46) are given in Table 2 for four different droplet sizes. One can observe a perfect match between analytical and numerical results with a deviation less than 1%.

4.2.3. Qualitative results for evaporating droplets

In order to assess the method of modelling the source term in the continuity equation, the time dependent evolution of the averaged pressure inside the liquid compared to that inside the gaseous phase was investigated. With an incorrect formulation of this source, the pressure correction leads to non-physical oscillations inside the pressure field.
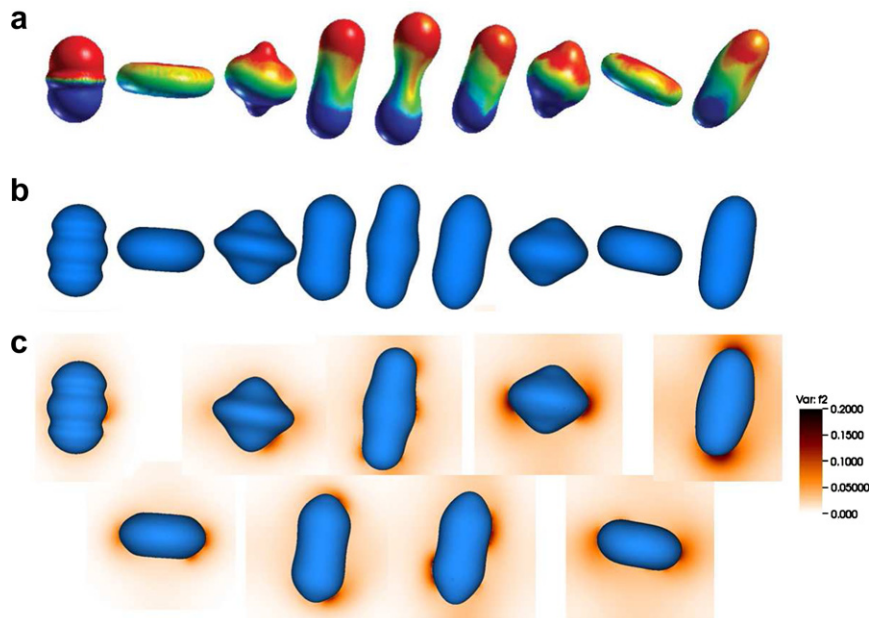

Fig. 10. Binary droplet collision for $We = 20$, $\chi = 0.05$; (a) results by [24], (b) own calculations without evaporation, (c) with evaporation (water), $T = 293$ K.
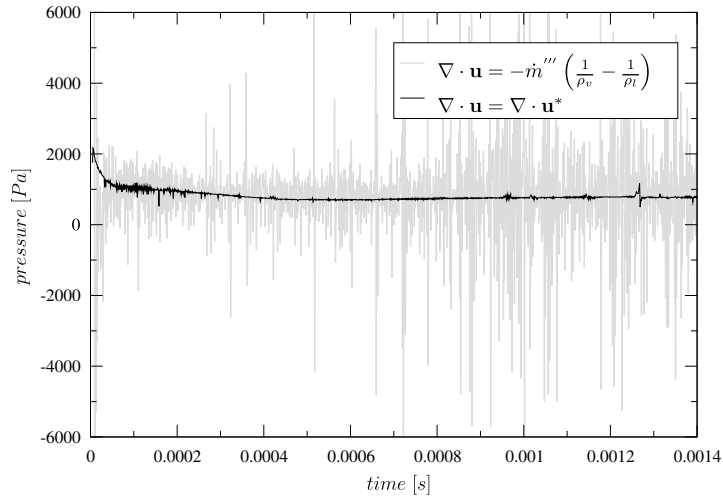
Fig. 11. Time dependent evolution of averaged pressure.

For testing purposes, calculations employing the formulation given in Eq. (16) were performed and the pressure evolution was compared to that calculated by the present method. The results shown in Fig. 11 clearly demonstrate the big difference between the smooth curve of the new model and the oscillating pressure development when using Eq. (16).

Besides their general undesirability, these oscillations can pose a threat to the whole algorithm due to the dependence of the vapour source on the pressure. The formulation of $\dot{m}'''$ uses the static pressure in order to determine the local vapour mass fraction at the surface. An incorrect prediction of the static pressure caused by an incorrect (too large) source in the continuity equation can therefore lead to an overprediction of the vapour source because a higher vapour mass fraction at the surface is calculated by Eqs. (25) and (26) which in turn generates an even higher source in the continuity equation, making the problem worse.

The improvement in terms of a smooth temporal development can also be observed by comparing the computed Sherwood number with results obtained in [7]. Sh is defined by

$$Sh = \frac{D\beta}{\mathcal{D}_{\text{vg}}}, \tag{47}$$

where D denotes the diameter of a volume equivalent droplet and β is the mass transfer coefficient. The development of Sh, taken from simulations of the Ranz and Marshall experiments [25, see below] for a Reynolds number of $Re_{\text{D}} = 96$, is shown in Fig. 12 for both models. Again, the smooth Sh-curve predicted by the present model is in contrast to the prediction of the former model by Hase, which is superposed by high frequency oscillations.

4.2.4. Droplet evaporation with low mass transfer rates

The method was quantitatively validated for the case of low mass transfer rates by simulating the well documented experiments conducted by Ranz and Marshall [25]. Their correlation

$$Sh = 2 + 0.6Re_{\text{D}}^{1/2}Sc^{1/3} \tag{48}$$

with $Sc = \mu/\mathcal{D}_{\text{vg}}$ being the Schmidt number, has often been used in the past. A more recent experimental investigation on evaporating droplets was done by Schwarz and Smolik [39]; their results for Sh are on a lower level compared to those of Ranz and Marshall. Kulmala and Vesala developed the correlation

$$Sh = 2.009 + 0.514Re_{\text{D}}^{1/2}Sc^{1/3} \tag{49}$$

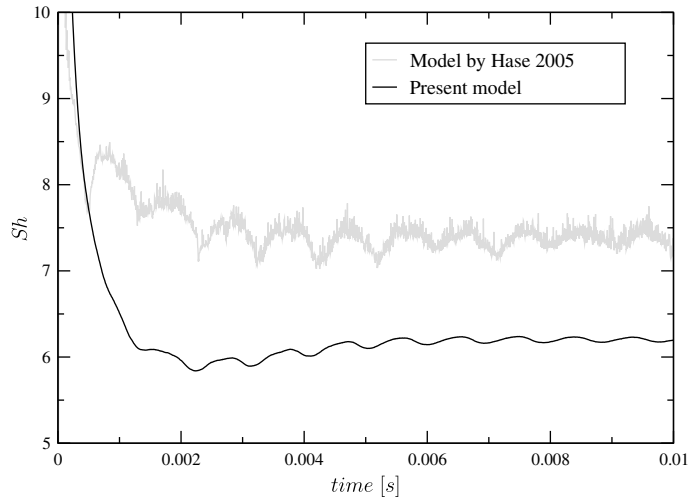on basis of the experimental data by Schwarz and Smolik [18].

Fig. 12. Temporal evolution of Sherwood Number; comparison with model by Hase [7].

The comparison of the given correlations, the experimental results and the numerical results produced by the present method for a Schmidt number of $Sc = \mu/(\rho \mathcal{D}_{vg}) = 0.63$ and a Prandtl number of $Pr = \mu c_p/\lambda = 0.72$ is shown in Fig. 13. The simulations were performed on three different grids (coarse: $64 \times 32 \times 32$ cells, medium: $128 \times 64 \times 64$ cells, fine: $256 \times 128 \times 128$ cells) using two symmetry planes. Material properties were chosen according to the experiments of Ranz and Marshall, causing a density ratio of $\rho_l/\rho_g \approx 830$ and a viscosity ratio of $\mu_l/\mu_g \approx 75$. A summary of the numerical results is presented in Table 1. The numerical results shown in Fig. 13 are those computed on the fine grid.

With increasing Reynolds number, there is a growing deviation between the correlation by Ranz and Marshall (Eq. (48)) and the numerically obtained results. However, this deviation is smaller if one considers the actual evaporation rates as they are given in Table 1 instead of the Sherwood number. This is likely due to a different selection of the material properties that occur in the determination of the dimensionless quantities.

Furthermore, the numerical results are in good agreement with the data measured by Schwarz and Smolik and the correlation of Kulmala and Vesala with a maximum deviation of about 6% for the highest considered Reynolds number $Re_D = 132.4$.
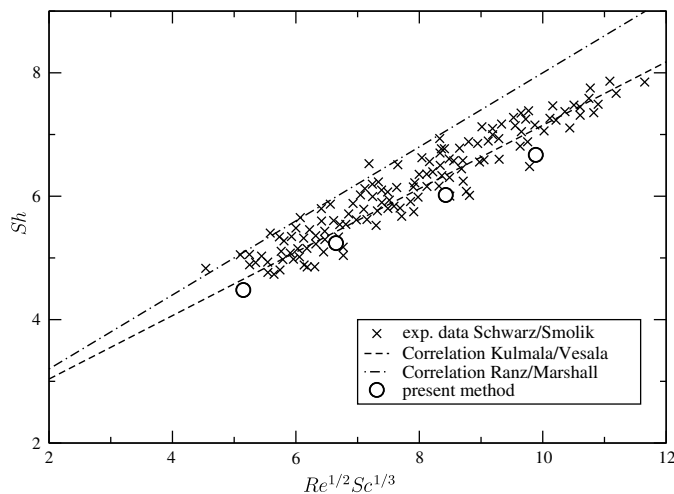

Fig. 13. Comparison of calculated Sh-results, experimental results and correlations from the literature for low mass transfer rates.

Looking at the computed Sherwood numbers on the three different grids (Table 1), the need of a high resolution in order to sufficiently resolve the boundary layer becomes apparent. This need is of growing importance for higher Reynolds numbers where the boundary layer gets thinner. The deviation between the Sherwood numbers calculated on the medium and the fine grid is therefore augmenting if Re_D increases. This implies that even the fine grid, consisting of approximately 4 million cells and giving a spatial resolution of 20 μm, still does not provide a completely sufficient resolution for the given problem. This fact is also emphasized by the computed *grid convergence index* GCI [37] which is used in order to express the reliability of the given results.

In Table 1, values of *Sh* that have been extrapolated using the method proposed by Richardson [31] are presented, too. Those values show a maximum deviation compared to the correlation by Kulmala and Vesala of less then 4%.

4.2.5. Droplet evaporation with high mass transfer rates

For the case of high mass transfer rates, numerical calculations were done and the obtained Sherwood numbers were compared to the correlation given by Renksizbulut et al. [29]:

$$Sh_{film}(1 + B_M)^{0,7} = 2 + 0.87Re_m^{1/2}Sc_{film}^{1/3}. \tag{50}$$

The subscript film indicates that the material properties have been taken at film conditions and Re_m is the "mixed" Reynolds number consisting of properties chosen both at film condition and in the free flow: $Re_m = D\rho_\infty u_\infty / \mu_{film}$. The parameter $B_M = (X_{v,surface} - X_{v,\infty})/(1 - X_{v,surface})$ denotes the mass transfer number. Due to the limitation to constant properties, all material properties (except those for the liquid) used in the present simulation were chosen at film conditions. Calculations on different grids were performed in an analogous way to that already described for the case of low mass transfer rates. The results for a water droplet at $T_1 = 90$ °C in a hot, dry air stream ($T_\infty = 800$ °C) are presented in Fig. 14. The density ratio for this case is $\rho_l/\rho_g \approx 1980$, the viscosity ratio is $\mu_l/\mu_g \approx 9$, the surface tension is $\sigma = 61 \times 10^{-3}$ N/m and the binary diffusion coefficient is $\mathcal{D}_{vg} = 1.26 \times 10^{-4}$ m²/s. The results are in very good agreement with the given correlation. This confirms the ability of the presented method to capture the thickening of the concentration boundary layer due to the Stefan flow and to reflect the emerging self-inhibition of evaporation that takes place in the case of high mass transfer rates.

4.3. Deformed droplet at high Reynolds and Weber number

In order to demonstrate the power of the present code FS3D, the behaviour of a deformed droplet in an air stream was investigated. The three-dimensional numerical setup presented in Section 4.1 was used therefore as well, that is freeslip condition for the lateral walls without symmetry planes, a uniform inflow condition of dry air ($f_2 = 0$) at the left side of the domain and a damping zone at the outlet. The droplet fluid is water at a

Table 1
Results of the simulation of experiments by Ranz and Marshall

|	Grid	$Re = 35.9$	$Re = 59.9$	$Re = 96.2$	$Re = 132.4$
Sh (−)	Coarse	4.38	4.92	5.45	5.77
Sh (−)	Medium	4.42	5.14	5.85	6.37
Sh (−)	Fine	4.44	5.21	6.03	6.67
$\epsilon_{R\&M}$ (%)	Fine	12.75	13.02	14.55	15.91
$\epsilon_{Kulmala}$ (%)	Fine	4.62	4.00	4.90	5.94
ϵ (%)	Medium/fine	0.45	1.34	2.99	4.50
GCI (%)	Fine	2.88	0.78	3.05	5.60
Sh (−)	Richardson	4.54	5.24	6.18	6.97
$\epsilon_{R\&M}$ (%)	Richardson	10.79	12.52	12.42	12.13
$\epsilon_{Kulmala}$ (%)	Richardson	2.48	3.45	2.54	1.71
$\dot{m}$ (kg/s × 10^{-6})	Fine	2.68	3.02	3.66	3.98
$\epsilon_{\dot{m},R\&M}$ (%)	Fine	3.25	5.63	5.67	10.56

Table 2
Periodic time of droplet oscillations; comparison between numerical and analytical results

	Mass (g)	T (Eq. (46)) (s)	T (numerics) (s)	Deviation (%)
1	4.9469×10^{-5}	0.896×10^{-3}	0.895×10^{-3}	-0.11
2	9.8210×10^{-5}	1.262×10^{-3}	1.259×10^{-3}	-0.24
3	1.9545×10^{-4}	1.781×10^{-3}	1.783×10^{-3}	0.11
4	3.9575×10^{-4}	2.534×10^{-3}	2.544×10^{-3}	0.39
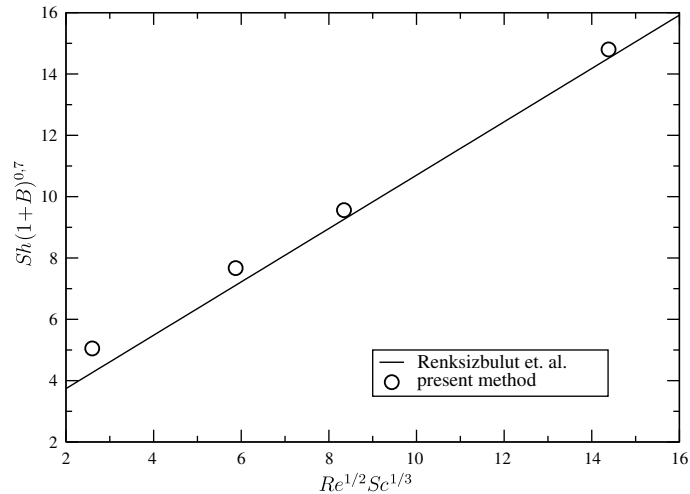
Fig. 14. Comparison of calculated Sh-results and the correlation by Renksizbulut et al. for high mass transfer rates.

temperature of $T_1 = 70\ ^\circ$C inside a dry air flow with $T_\infty = 90\ ^\circ$C, leading to a density ratio of $\rho_1/\rho_g \approx 980$ and a viscosity ratio of $\mu_1/\mu_g \approx 19$. With the uniform velocity $u_\infty = 15$ m/s as the inflow boundary condition and a diameter of the initially spherical droplet of $D = 0.21$ cm, the droplet Reynolds number results to $Re_D = 1495$ and the Weber number to $We = \rho_g u_\infty^2 D/\sigma = 7.3$ ($\sigma = 64.9 \times 10^{-3}$ N/ m). The calculation was performed on a grid consisting of $128 \times 128 \times 128$ cells on one NEC SX-8 vector processor lasting about 15 hours for a considered realtime of 40 ms.
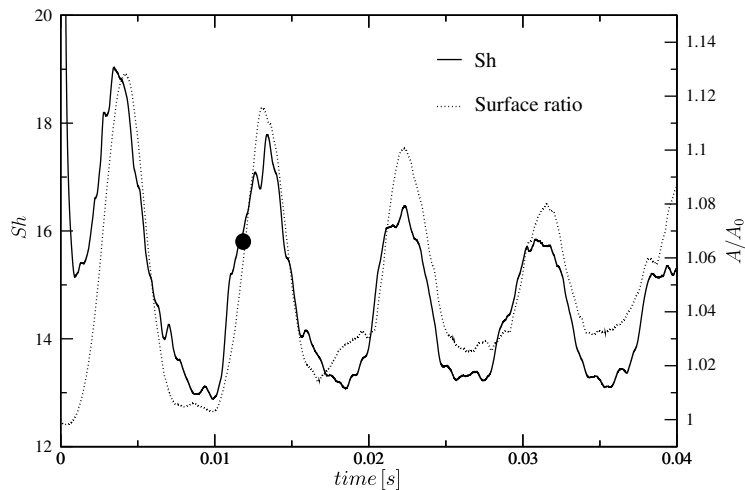

Fig. 15. Temporal development of surface ratio A/A_0 and Sherwood number.
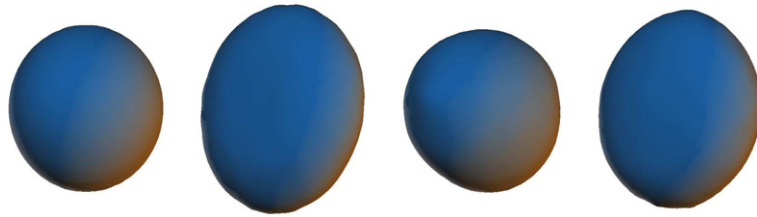
Fig. 16. Droplet at $t = 0$, 5, 8 and 12 ms.

The temporal development of the deformation, expressed as the ratio of the actual surface to the surface of the initial sphere A/A_0, and the Sherwood number are shown in Fig. 15. Due to the initial condition of dry air, the initial gradient of the vapour mass fraction at the surface is infinite and consequently the initial Sherwood number is infinite, too. The sudden start of the air flow – comparable to experiments conducted in shock tubes – leads to a big deformation of the droplet at the beginning of the simulation producing a quite oblate shape. The droplet then starts oscillating whereas the maximum deformation decays with increasing number of oscillations. The shape of the droplet at different time steps can be seen in Fig. 16 for $t = 0$ ms, $t = 5$ ms, $t = 8$ ms and $t = 12$ ms. As was already observed in [10] for the heat transfer, the occurrence of the maximum mass transfer coincides with the highest deformation of the droplet.

For the further investigation of the flow, concentration and temperature fields around and inside the droplet, plots will be shown for the time marked with the filled circle in Fig. 15 ($t = 12$ ms).

Fig. 17 depicts the flow field around the droplet, where the complex three-dimensional flow behind the droplet is remarkable and its unsteady, chaotic character becomes evident. Looking at the velocity magnitude indicated by the color of the stream line ribbons, a recirculation zone behind the droplet with very low velocities can be observed. The fluid exchange between this zone and the surrounding gas is rather low, leading to higher concentrations of vapour and lower temperatures (see below).
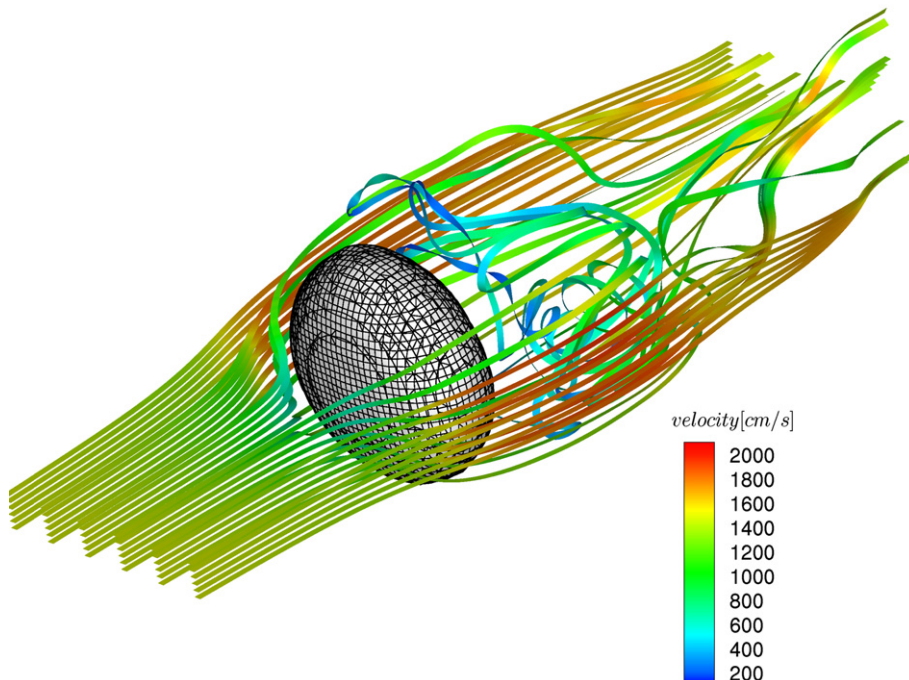
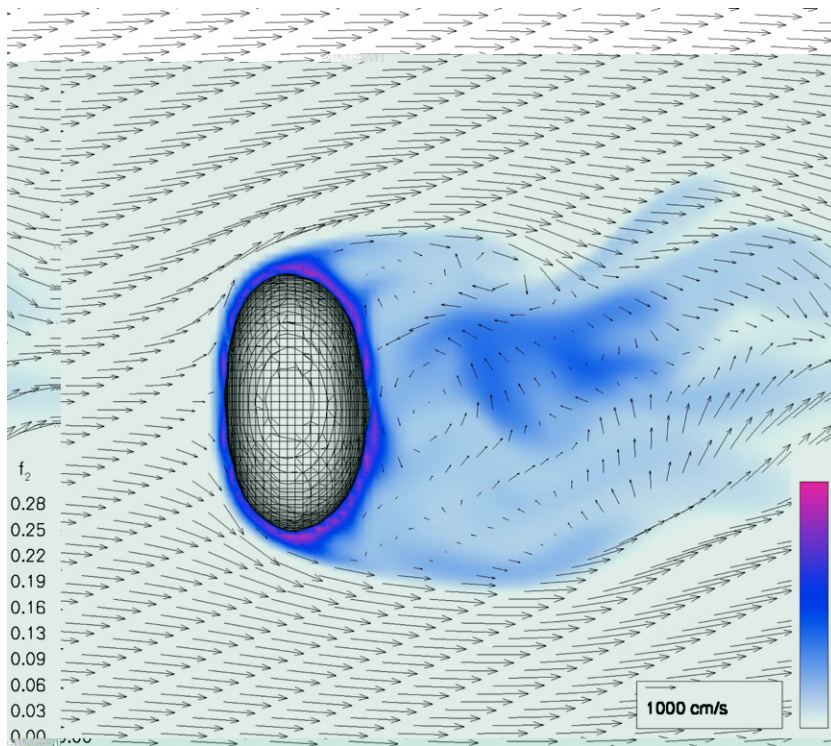Fig. 17. Flow field around the droplet at $t = 12$ ms.

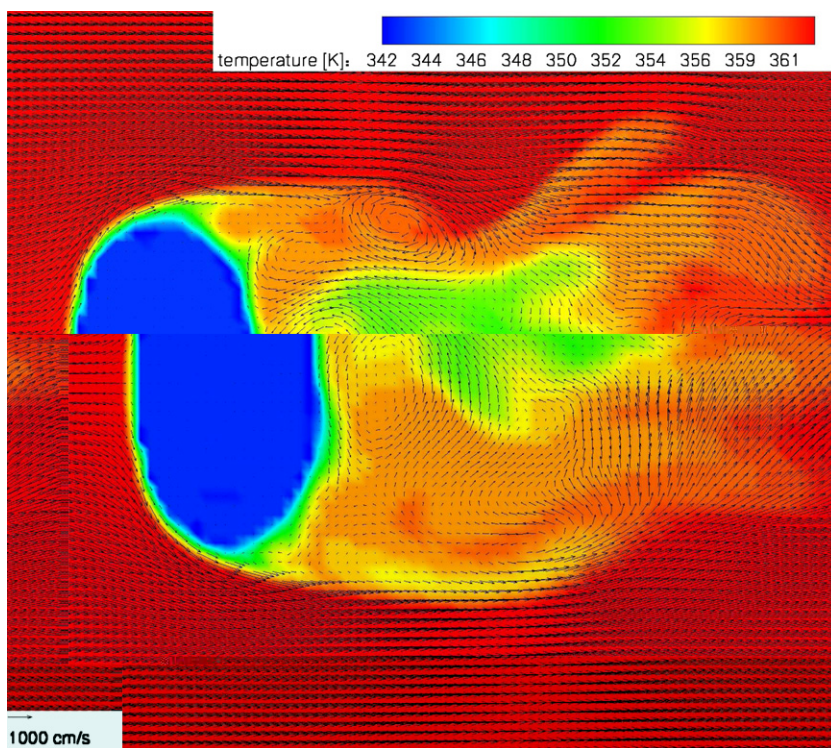Fig. 18. Vapour distribution shown by VOF variable f_2 at $t = 12$ ms.

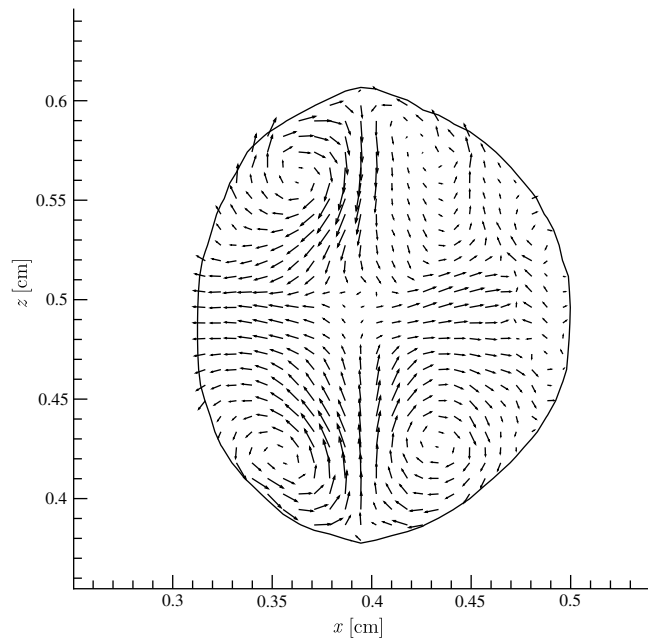Fig. 19. Temperature distribution inside and around the droplet at $t = 12$ ms.

Fig. 20. Velocity field inside the droplet.

In order to assess the distribution of vapour inside the domain, the VOF variable f_2 and the tangential vectors of velocity are depicted in Fig. 18 on a slice through the centre of the droplet. The highest concentration of vapour can be observed directly at the surface of the droplet, as expected. Furthermore, there is a zone with quite high values of f_2 in the wake of the droplet due to recirculation as already stated above. Generally one has to bear in mind that only a snapshot is shown and the presented distribution changes rapidly. However, the figures give a good impression of the phenomena taking place.

The temperature distribution inside and around the droplet is shown in Fig. 19 on the same slice through the droplet centre already used above. The temperature field inside the droplet is homogeneous with slight gradients near the droplet surface. This seems plausible and is a result of the mixing due to the flow field inside the droplet. Considering the temperature field around the droplet, one clearly sees that the convective domination of the problem leads to a very similar distribution compared to that of the vapour concentration.

Finally the velocity field inside the droplet is presented in Fig. 20. There are two vortex pairs that are generated by the outer flow adjacent to the droplet surface. These vortex structures lead to a very strong mixing of the fluid as already stated above with regard to the temperature distribution inside the droplet.

5. Conclusion

Evaporation of droplets in an air flow has been studied numerically by using the in house code FS3D. The match of the calculated Sherwood numbers with data from the literature proves the ability of the presented vapour source formulation to account for flows with low and high mass transfer rates. This formulation is accompanied by the method of calculating the velocities of the gaseous and the liquid phase at the interface, allowing to consider the Stefan flow in a correct way. The computation of the source for the continuity equation results in a smooth temporal developing of the pressure in contrast to pressure oscillations that occur when using a formulation of this source found in literature in the framework of the presented method.

The method was used to study the behaviour of a strongly deformed water droplet at high Reynolds and Weber numbers. Certain interesting physical processes were identified, including the complex three-dimensional flow in the wake of the droplet, its transient behaviour and the relation between deformation and Sherwood number.

Improvements still to implement involve the use of temperature dependent material properties for flows with a big temperature range as well as local grid refinement at the interface in order to significantly reduce the numerical costs for problems with thin boundary layers.

Acknowledgment

Appendix A. Wagner equation

The vapour pressure $p_{v,sat}$ at the interface is calculated using the Wagner equation as proposed by [26]. The equation for the reduced vapour pressure $p_{v,sat,r} = p_{v,sat}/p_c$ (p_c: critical pressure) reads

$$p_{v,sat,r} = \frac{a\tau + b\tau^{1.5} + c\tau^3 + d\tau^6}{T_r}, \tag{A.1}$$

where $T_r = T/T_c$ is the reduced temperature (T_c: critical temperature), $\tau = 1 - T_r$ and a, b, c, d are material constants. All properties for different fluids are provided by [26].

References

[1] J. Brackbill, D. Kothe, C. Zemach, A continuum method for modelling surface tension, Journal of Computational Physics 100 (1992) 335–354.

[2] M.R. Davidson, M. Rudman, Volume-of-fluid calculation of heat or mass transfer across deforming interfaces in two-fluid flow, Numerical Heat Transfer 41 (2002) 291–308.

[3] D. Enright, R. Fedkiw, J. Ferziger, I. Mitchell, A hybrid particle level set method for improved interface capturing, Journal of Computational Physics 183 (2002) 83–116.

[4] R. Fedkiw, T. Aslam, B. Merriman, S. Osher, A non-oscillatory Eulerian approach to interfaces in multimaterial flows (the ghost fluid method), Journal of Computational Physics 152 (1999) 457–492.

[5] F. Gibou, L. Chen, D. Nguyen, S. Banerjee, A level set based sharp interface method for the multiphase incompressible Navier–Stokes equations with phase change, Journal of Computational Physics 222 (2007) 536–555.

[6] F. Harlow, J. Welch, Numerical calculation of time-dependent viscous incompressible flow of fluid with free surface, Physics of Fluids 8 (12) (1965) 2182–2189.

[7] M. Hase, Numerische berechnung dreidimensionaler transportvorgänge an angeströmten, sich verformenden tropfen, Ph.D. thesis, Universität Stuttgart, 2005.

[8] M. Hase, B. Weigand, Numerical study of the temperature field of unsteady moving droplets and of the surrounding gas, in: Proceedings of ILASS-Europe Conference, Zuerich, 2001.

[9] M. Hase, B. Weigand, Numerical simulation of 3D unsteady heat transfer at strongly deformed droplets at high Reynolds numbers, in: High-Performance Computing in Science and Engineering, Springer-Verlag, 2003, pp. 255–266.

[10] M. Hase, B. Weigand, Transient heat transfer of deforming droplets at high Reynolds numbers, International Journal of Numerical Methods in Heat and Fluid Flow 14 (2004) 85–97.

[11] R.J. Haywood, M. Renksizbulut, G.D. Raithby, Numerical solution of deforming evaporating droplets at intermediate Reynolds numbers, Numerical Heat Transfer 26 (1994) 253–272.

[12] R.J. Haywood, M. Renksizbulut, G.D. Raithby, Transient deformation and evaporation of droplets at intermediate Reynolds numbers, International Journal Heat Mass Transfer 37 (1994) 1401–1409.

[13] C. Hirt, B. Nichols, Volume of fluid (VOF) method for the dynamics of free boundaries, Journal of Computational Physics 39 (1981) 201–225.

[14] R.-T. Jung, T. Sato, Numerical simulation of high schmidt number flow over a droplet by using moving unstructured mesh, Journal of Computational Physics 203 (2005) 221–249.

[15] D. Juric, G. Tryggvason, Computations of boiling flows, International Journal of Multiphase Flow 24 (3) (1998) 387–410.

[16] W. Kays, M. Crawford, B. Weigand, Convective Heat and Mass Transfer, fourth ed., McGraw-Hill, New York, 2005, 1221 Avenue of the Americas.

[17] D.B. Kothe, Perspective on Eulerian finite volume methods for incompressible interfacial flows, in: Free Surface Flows, Springer-Verlag, 1998, pp. 267–331.

[18] M. Kulmala, T. Vesala, Mass transfer from a drop – ii. Theoretical analysis of temperature dependent mass flux correlation, International Journal of Heat and Mass Transfer 38 (1995) 1705–1708.

[19] B. Lafaurie, C. Nardone, R. Scardovelli, S. Zaleski, G. Zanetti, Modelling merge and fragmentation in multiphase flows with SURFER, Journal of Computational Physics 113 (1994) 134–147.

[20] H. Lamb, Hydrodynamics, Cambridge University Press, 1957.
[21] F. Maichle, B. Weigand, K. Trackl, B. Wiesler, Improving car air conditioning systems by direct numerical simulation of droplet-wall interaction phenomena, in: Proceedings of the Nineth International Conference on Liquid Atomization and Spray Systems (ICLASS).
[22] A.F. Mills, Mass Transfer, Prentice Hall, 2001.
[23] N. Nikolopoulos, A. Theodorakakos, G. Bergeles, A numerical investigation of the evaporation process of a liquid droplet impinging onto a hot substrate, International Journal of Heat and Mass Transfer 50 (2007) 303–319.
[24] Y. Pan, K. Suga, Numerical simulation of binary liquid droplet collision, Physics of Fluids 17 (2005), Articleid 082105.
[25] W.E. Ranz, W.R. Marshall, Evaporation from drops part ii, Chemical Engineering Progress 48 (1952) 173–180.
[26] R. Reid, J. Prausnitz, B. Poling, Properties of Gases and Liquids, fourth ed., McGraw-Hill, 1986.
[27] M. Renksizbulut, M. Bussmann, Multicomponent droplet evaporation at intermediate Reynolds numbers, International Journal of Heat and Mass Transfer 36 (11) (1993) 2827–2835.
[28] M. Renksizbulut, R. Haywood, Transient droplet evaporation with variable properties and internal circulation at intermediate Reynolds numbers, International Journal Multiphase Flow 14 (2) (1988) 189–202.
[29] M. Renksizbulut, R. Nafziger, X. Li, A mass transfer correlation for droplet evaporation in high-temperature flows, Chemical Engineering Science 46 (1991) 2351–2358.
[30] M. Renksizbulut, M.C. Yuen, Numerical study of droplet evaporation in a high-temperature stream, Journal of Heat Transfer 105 (1983) 389–397.
[31] L.F. Richardson, The deferred approach to the limit, Transactions of the Royal Society of London 226 (1927) 299–361.
[32] W. Rider, D. Kothe, Reconstructing volume tracking, Journal of Computational Physics 141 (1998) 112–152.
[33] M. Rieber, Numerische modellierung der dynamik freier grenzflächen in zweiphasenströmungen, Ph.D. thesis, Universität Stuttgart, 2004.
[34] M. Rieber, A. Frohn, Navier–Stokes simulation of droplet collision dynamics, in: Proceedings of the Seventh International Symposium on Computational Fluid Dynamics, 1997.
[35] M. Rieber, A. Frohn, A numerical study on the mechanism of splashing, International Journal of Heat and Fluid Flow 20 (1999) 455–461.
[36] M. Rieber, F. Graf, M. Hase, N. Roth, B. Weigand, Numerical simulation of moving spherical and strongly deformed droplets, in: Proceedings ILASS-Europe, Darmstadt, 2000.
[37] P.J. Roache, Perspective: a method for uniform reporting of grid refinement studies, Journal of Fluids Engineering 116 (1994) 405–413.
[38] W. Sander, B. Weigand, Direct numerical simulation of primary breakup phenomena in liquid sheets, in: High-Performance Computing in Science and Engineering, Springer-Verlag, 2006, pp. 223–236.
[39] J. Schwarz, J. Smolik, Mass transfer from a drop – i. Experimental study and comparison with existing correlations, International Journal of Heat and Mass Transfer 37 (1994) 2139–2143.
[40] G. Son, V. Dhir, Numerical simulation of film boiling near critical pressures with a level set method, Journal of Heat Transfer 120 (1998) 183–192.
[41] M. Sussman, A second order coupled level set and volume-of-fluid method for computing growth and collapse of vapour bubbles, Journal of Computational Physics 187 (2003) 110–136.
[42] M. Sussman, E.G. Puckett, A coupled level set and volume-of-fluid method for computing 3d and axisymmetric incompressible two-phase flows, Journal of Computational Physics 162 (2000) 301–337.
[43] M. Sussman, P. Smereka, S. Osher, A level-set approach for computing solutions to incompressible two-phase flow, Journal of Computational Physics 114 (1994) 146–159.
[44] S. Tanguy, T. Menard, A. Berlemont, A level set method for vaporizing two-phase flows, Journal of Computational Physics 221 (2007) 837–853.
[45] S.O. Unverdi, G. Tryggvason, A front-tracking method for viscous, incompressible, multi-fluid flows, Journal of computational physics 100 (1992) 25–37.
[46] S. Welch, J. Wilson, A volume-of-fluid based method for fluid flows with phase change, Journal of Computational Physics 160 (2000) 662–682.